

Mask aspects of EUVL imaging at 27nm node and below

Natalia Davydova^{a,*}, Eelco van Setten^a, Sang-In Han^d,
Mark van de Kerkhof^a, Robert de Kruif^a, Dorothe Oorschot^a, John Zimmerman^e, Ad Lammers^a, Brid
Connolly^f, Frank Driessen^a, Anton van Oosten^a,
Mircea Dusa^b, Youri van Dommelen^d, Noreen Harned^e
Jiong Jiang^c, Wei Liu^c, Hoyoung Kang^c, Hua-yu Liu^c

^aASML Netherlands B.V., De Run 6501, 5504 DR Veldhoven, The Netherlands

^bASML Belgium bvba., Kapeldreef 75, 3001 Leuven, Belgium

^cBrion Technologies Incorporated, 4211 Burton Drive, Santa Clara, CA 95054, USA

^dASML Albany, 25 Corporate Circle, Suite 120, Albany, NY 12203, USA

^eASML Wilton, 77 Danbury Road, Wilton, CT 06897, USA

^fToppan Photomasks, INC, Rähnitzer Allee 9, 01109 Dresden, Germany

ABSTRACT

EUVL requires the use of reflective optics including a reflective mask. The mask consists of an absorber layer pattern on top of a reflecting multilayer, tuned for 13.53 nm. The EUVL mask is a complex optical element with many parameters contributing the final wafer image quality. Specifically, the oblique incidence of light, in combination with the small ratio of wavelength to mask topography, causes a number of effects which are unique to EUV, such as an HV CD offset. These so-called shadowing effects can be corrected by means of OPC, but also need to be considered in the mask stack design.

In this paper we will present an overview of the mask contributors to imaging performance at the 27 nm node and below, such as CD uniformity, multilayer and absorber stack composition, thickness and reflectivity. We will consider basic OPC and resulting MEEF and contrast. These parameters will be reviewed in the context of real-life scanner parameters both for the NXE:3100 and NXE:3300 system configurations.

The predictions will be compared to exposure results on NXE:3100 tools, with NA=0.25 for different masks. Using this comparison we will extrapolate the predictions to NXE:3300, with NA=0.33.

Based on the lithographic investigation, expected requirements for EUV mask parameters will be proposed for 22 nm node EUV lithography, to provide guidance for mask manufacturers to support the introduction of EUV High Volume Manufacturing.

Key words: EUV, lithography, imaging, photomask, reticle, NXE

1. INTRODUCTION

EUVL requires the use of reflective optics including a reflective mask. The mask consists of a substrate made of Low Thermal Expansion Material (LTEM), a reflective multilayer consisting of 40 to 50 bi-layers of molybdenum and silicon and 50-100 nm thick absorber with anti-reflective coating. EUV light falls under the chief ray angle of 6 degrees to the mask for NXE:3100 and NXE:33xx systems. Angles in illumination cone (full NA) varies in the range 2 to 10 degrees for NXE:3100 and 1 to 11 degrees for NXE:33xx. The reflectivity spectrum of the mask multilayer must be tuned to the spectrum of projection optics of a lithography tool.

An EUV mask is a complex optical element with many more parameters that impact the final wafer CDU than the CD uniformity of the patterned features. The multilayer (ML) stack needs to be tightly controlled for peak reflectivity and centroid wavelength variations. The absorber stack needs to have a uniform and precisely determined height across the wafer to minimize CD errors while taking the flare level from EUV reflection from the absorber into account. Furthermore, the oblique incidence of light in combination with the wavelength that is relatively small compared to the

* natalia.davydova@asml.com

mask topography causes a number of effects which are unique to EUV, such as an HV CD offset and an orientation dependent pattern placement error. These so-called shadowing effects can be corrected by means of OPC, but also need to be considered in the mask stack design. The imaging performance (Exposure Latitude, Mask Error Enhancement Factor) can be optimized by an integral approach, taking the absorber thickness and mask bias into account.

In this paper we will look into the impact of multilayer performance on imaging in terms of centroid wavelength tuning, absorber height and bias impact on imaging for 27 nm dense L/S in resist by means of wafers exposed on NXE:3100. Rigorous simulations are performed to evaluate the possibilities for mask stack optimization for the NXE:3300 with 22 nm node. Furthermore, we will look at the impact of EUV absorber reflectivity on CD uniformity due to image border reflections at the edges of the field and possible correction methods by means of mask OPC.

2. MULTILAYER CENTROID WAVELENGTH OPTIMIZATION

Multilayer is characterized by its reflectivity spectrum through EUV wavelength for different angles of incidence (AOI) to the mask. On Figure 1 a measured reflectivity spectrum of a multilayer is shown for AOI of 6 degrees characterized by centroid wavelength, peak reflectivity and full width at half maximum. This spectrum was also successfully simulated in KLA-Tencor ProLith 3.2 software using a rigorous Maxwell model and a detailed stack.

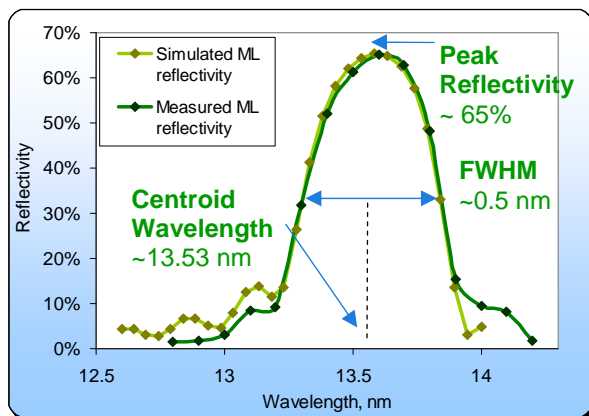


Figure 1 A measured and simulated multilayer reflectivity spectrum characterized by centroid wavelength, peak reflectivity and full width at half maximum (FWHM).

A multilayer stack with 40-layers was optimized in order to match *peak reflectivity* and *full width at half maximum* (FWHM) of a measured multilayer reflectivity spectrum (*centroid wavelength* can be easily matched by scaling of the ML stack thickness - see below). For this purpose thicknesses of two MoSi₂ intermixing layers were optimized. The resulting ML stack has the following thicknesses: 2.497 nm Si, 0.799 nm MoSi₂, 1.897 nm Mo and 1.837 nm MoSi₂ with the total ML period of 7.03 nm. The accuracy of the matching was 0.26% for peak reflectivity and 0.0002 nm for FWHM. The usage of the intermixing layers in simulation seems to be unavoidable because otherwise peak reflectivity and FWHM of the spectrum are largely overestimated. The actual presence of the MoSi₂ intermixing layers was demonstrated in^[1] by means of transmission electron spectroscopy (XTEM) showing the intermixing layers with thickness of 0.6 nm on Mo top and 1.7 nm on Si top with the full ML period of 6.95 nm and Mo/Si ratio of 0.4. Notice that in our simulation we have kept the ratios between the layers thickness close to these experimental values, while the total ML period was 1.5% increased in order to match the centroid wavelength.

If angle of incidence to the mask or ML stack thickness vary, the reflectivity spectrum change and, in particular, the centroid wavelength is shifted. This shift was simulated using the calibrated ML stack described above (Figure 2). The centroid wavelength grows linearly as a function of ML stack thickness and decreases quadratically through the angle of incidence. This can be understood from a thin film interference approximation. Peak (and centroid) wavelength are determined by an optical path difference (OPD) corresponding to constructive interference. OPD is described by the following equation:

$$OPD = 2n_2d \cos \theta_2 = 2n_2d \sqrt{1 - \left(\frac{n_1}{n_2}\right)^2 \sin^2 \theta_1} \approx 2n_2d \left(1 - \frac{\theta_1^2}{2n_2^2}\right).$$

We assumed that incident angle θ_1 and refracted angle θ_2 are small. Refractive index n_1 of vacuum is 1 while n_2 is an effective refractive index for multilayer which is estimated to be 0.965 (from the slopes of simulated curves) close to the refractive index of MoSi₂ (0.969).

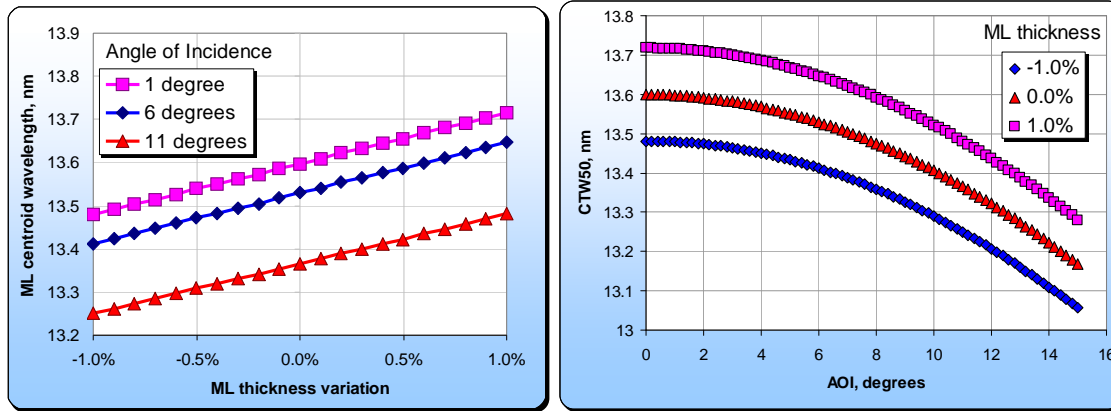


Figure 2 The centroid wavelength of ML reflectivity spectrum depends linearly on the ML stack thickness (left) and quadratically on the angle of incidence (right).

Having the linear relation between ML thickness and the centroid wavelength, we can easily vary the latter in simulation by changing the ML thickness / period while keeping ratios between the monolayers (gamma) constant. The ML is then fully described by its *nominal centroid wavelength* *ctw50* at the AOI of 6 degrees. For all simulations further ML with the period of 7.03 nm is used with the nominal ctw50 of 13.53 nm corresponding to a specification in ASML reticle manual.

Illumination in a EUV scanner has a certain bandwidth which must be taken into account in mask reflectivity calculations and imaging simulations. We will consider *broad band ML reflectivity* which is a convolution of scanner optics spectrum and ML spectrum as illustrated in Figure 3. Here the green curve represents ML reflectivity, the blue curve is a relative spectrum of the scanner optics (normalized to unit integral power) and the blue area is the convolution representing the broad band ML reflectivity.

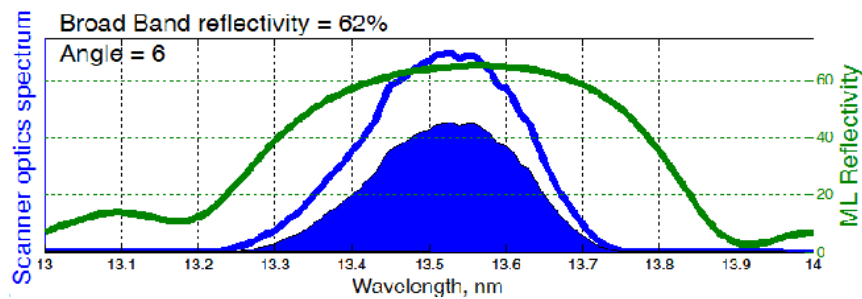


Figure 3 Broad band reflectivity of mask multilayer is a convolution of ML reflectivity spectrum and scanner source and optics spectrum.

The broad band mask reflectivity depends on illumination angle. It can be represented as a map in the pupil plane as shown in Figure 4 (see also^[2]). Average broad band reflectivity over the angles of incidence is determined by the particular illumination type.

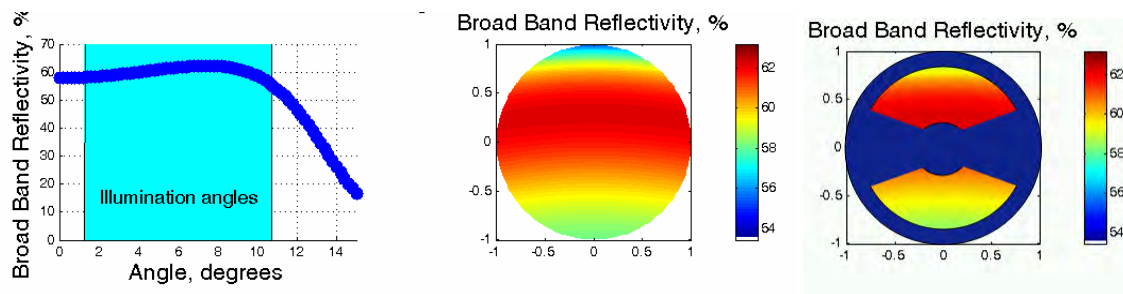


Figure 4 ML broad band reflectivity depends on light incidence angle (left). This is represented as a map in the pupil plane (middle). Average broad band reflectivity depends on illumination type (right).

If the mask is detuned relative to the scanner optics, the average broad band reflectivity drops. In addition, the range of reflectivity variation over the angles of incidence increases. This effect is called *mask induced apodization* which is defined as a range of the reflectivity variation normalized to maximal broad band reflectivity. Figure 5 illustrates dependence of the broadband reflectivity and the apodization on the mask centroid wavelength.

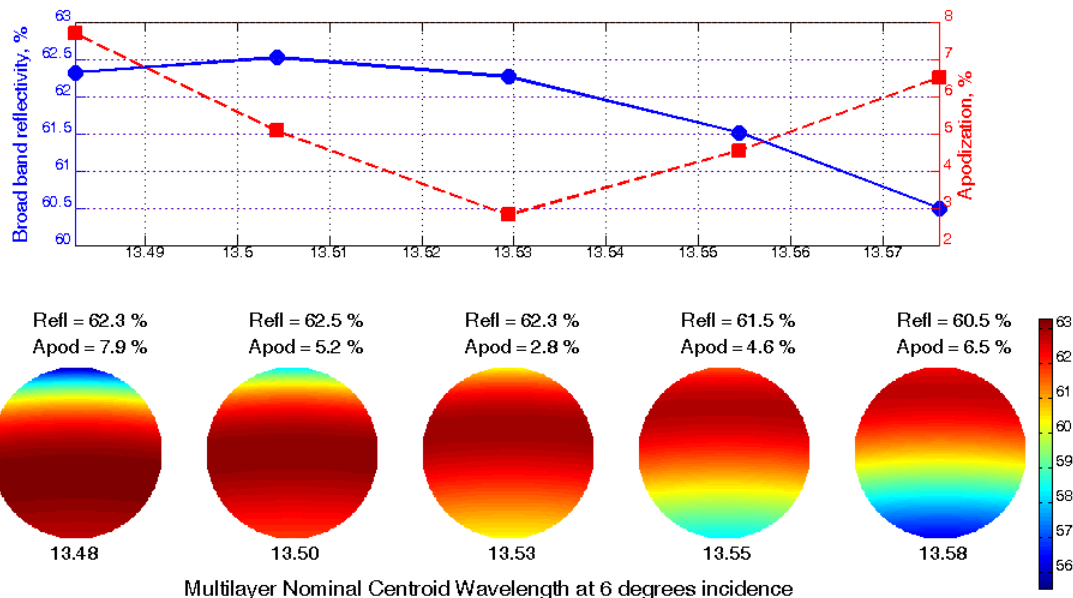


Figure 5 If the mask centroid wavelength is detuned w.r.t. the scanner optics, the average broad band reflectivity drops and apodization increases.

There is a near quadratic dependence of the average broad band reflectivity on the centroid wavelength as shown on Figure 6 (left). Therefore the reflectivity reaches maximum at a certain optimal wavelength, and also the sensitivity of reflectivity to the centroid wavelength and ML thickness variations over the blank is minimized at this wavelength. An average optimal centroid wavelength for different illumination types is calculated to be 13.52 nm for the maximal reflectivity metrics with ± 0.01 nm range for different illumination types. The reflectivity variation over the blank can be directly translated in the dose and CD variation (Figure 7, left).

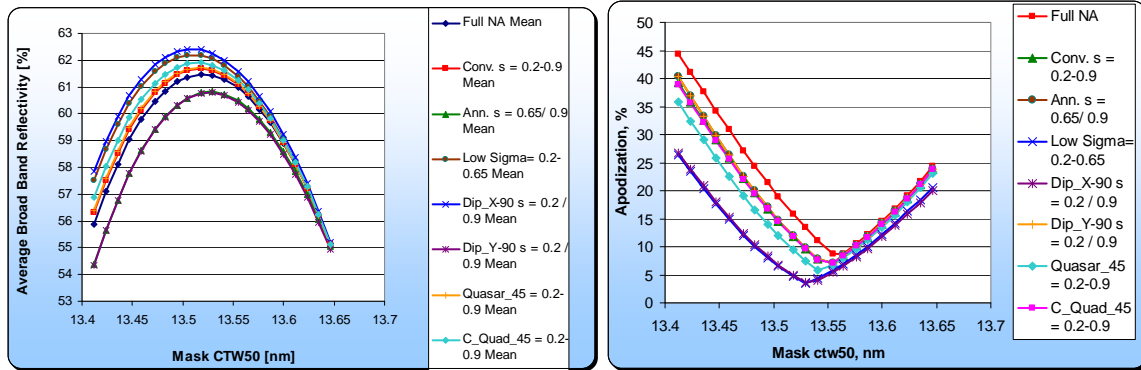


Figure 6 Broad band reflectivity (left) and apodization (right) have an optimal centroid wavelength.

The centroid wavelength can also be optimized based on apodization minimization as shown on Figure 6 (right). The average optimal ctw50 is 13.54 ± 0.01 in this case. Ctw50 variations over the blank are specified to be ± 0.02 nm that corresponds to maximal apodization of 17.2%. Notice that 22 nm node specifications can support up to 30% apodization. The apodization leads to diffraction orders imbalance that results in *mask induced telecentricity errors* and pattern displacement (Figure 7, right).

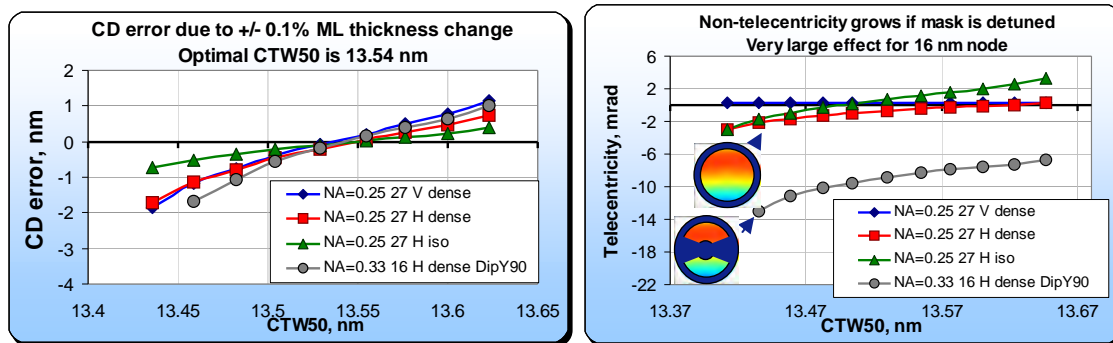


Figure 7 Reflectivity variation through the blank results in CD non-uniformity if ctw50 is detuned (left). The apodization results in diffraction order imbalance and telecentricity errors (right).

The simulation results shown on Figure 7 are performed for a single exposure wavelength and therefore preliminary. More detailed simulations of these imaging and overlay effects for 22 nm node and below will be performed.

3. ABSORBER OPTIMIZATION

EUV mask absorber has three dimensions: height, vertical and horizontal feature bias. All three dimensions can be optimized together to reach optimal imaging performance in contrast and exposure latitude. The exposure latitude has a global maximum in absorber height vs. bias space^[3]. This global maximum depends on illumination setting. It was also shown by means of simulations that thicker absorbers perform better for larger angular distribution $NA\sigma$ of illumination light for 27 nm node.

This result is confirmed by new simulations using the calibrated ML stack. The simulations are performed for 27 nm dense lines for three illumination settings: $NA=0.25 / \sigma=0.5$, $NA=0.25 / \sigma=0.8$ and $NA=0.33 / \sigma=0.9/0.2$. The results are shown in Figure 8 (left column). We see that for broader illumination EL maximum is shifted towards thicker absorber and larger biases.

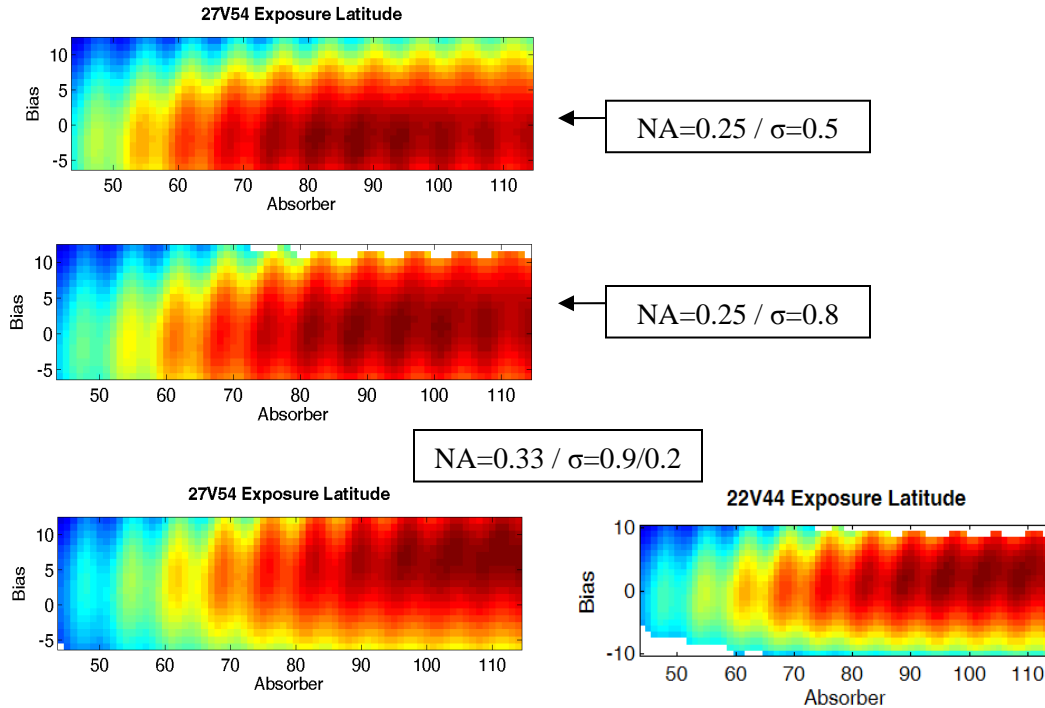


Figure 8 Exposure latitude has a global maximum in Absorber height vs. Bias space. This maximum is shifted towards thicker absorbers and larger biases for broader illumination settings $NA\sigma$ for 27 nm node (left column, from top to bottom). The optimal absorber thickness is smaller for 22 nm lines than for 27 nm (bottom row).

For $NA=0.33 / \sigma=0.9/0.2$, exposure latitude of 22 nm dense lines was also calculated (Figure 8, bottom right). The optimal absorber thickness becomes smaller for 22 nm node compared to 27 nm. Notice that the same full physical resist model is used in both cases for the comparison reason, while on practice a resist with a smaller diffusion length will presumably be used for 22 nm imaging.

The summary of the simulations is shown in Figure 9. The global absorber height and HV bias is shown for all cases. On practice there is no need to go to this global maximum for an acceptable imaging performance because the usage of thick absorber requires also higher exposure dose^[3]. But the values and trends show clearly that there is no urgent need to go to smaller absorber height for 22 nm imaging, though HV shadowing bias compensation on mask in case of thick absorber is a requirement.

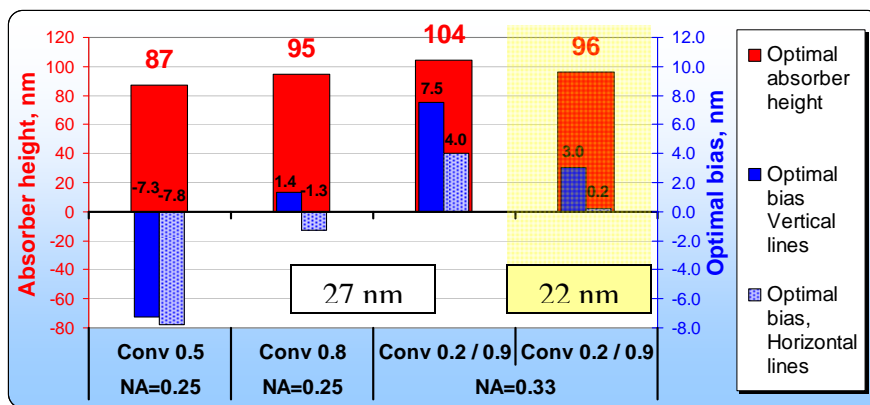


Figure 9 Absorber height, vertical and horizontal dense lines bias corresponding to maximal exposure latitude.

There is also a positive (almost linear) correlation between optimal absorber height and k_1' imaging factor, defined as $NA\sigma \cdot \text{half-pitch} / \lambda$ for 27 nm node (Figure 10). In other words, there is more absorber volume required for a better contrast if the light is distributed over a larger range of incident angles. For example, for NXE:3300 system with multiple illumination settings available, one may better choose thinner absorber for lower sigma and thicker absorber for larger sigma. We will follow on this subject in future work.

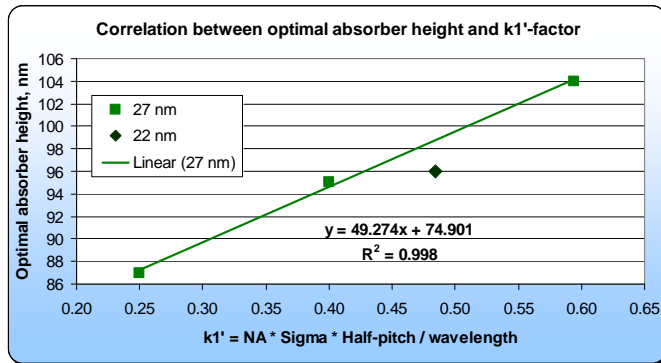


Figure 10 Correlation between the imaging factor $k_1' = NA\sigma \cdot \text{half-pitch} / \lambda$ and the optimal absorber height is shown.

4. EXPERIMENTAL DETERMINATION OF BEST ABSORBER THICKNESS

Following the EL-based optimization methodology, best bias was determined experimentally for two masks with similar layout and different absorber thicknesses: 55.4 nm and 70 nm. The masks were exposed on NXE:3100 scanner with $NA=0.25$ and $\sigma=0.8$ illumination settings. Two resist processes were used: 50 nm Shin-Etsu SEVR-140 resist with and without undercoat AL412. Exposure latitude and dose to size for a range of biases for 27 nm dense, semi-dense and isolated lines and 32 nm dense lines were measured.

Exposure latitude (EL) was used as a metric for bias optimization and it was calculated based on a calibrated full physical resist model. Figure 11 shows that EL is a quadratic-like function of mask bias and therefore can be maximized.

A similar experiment with four masks were already performed earlier^[3] on EUV Alpha tool with $NA=0.25$ and $\sigma=0.5$ illumination setting, showing growing exposure latitude from 13% to 20% for 27 nm dense lines through absorber height for masks with 44 nm, 55.4 nm and 58 nm absorber and drop of exposure latitude for 87 nm mask. Dose to size increases 23-25% for 27 nm dense lines and 35-36% for 32 nm dense lines between 44 nm and 87 nm absorber mask. The optimal bias has shown strong dependence on absorber height.

The results of the current NXE:3100 experiment are represented on Figure 12. Measured data show quadratic trends in most of the cases as well as simulated data. Exposure latitude for 70 nm absorber is ~2% absolute higher than of 55.4 nm absorber in both simulated and experimental data. However simulated and measured best biases do not match: in particular, best biases for (semi-) isolated features in simulations are positive while in measurements they are mostly negative. This might be related to system contribution (aberrations) of early EUV tools; in addition, no measured mask CD data were available for 70 nm absorber reticle.

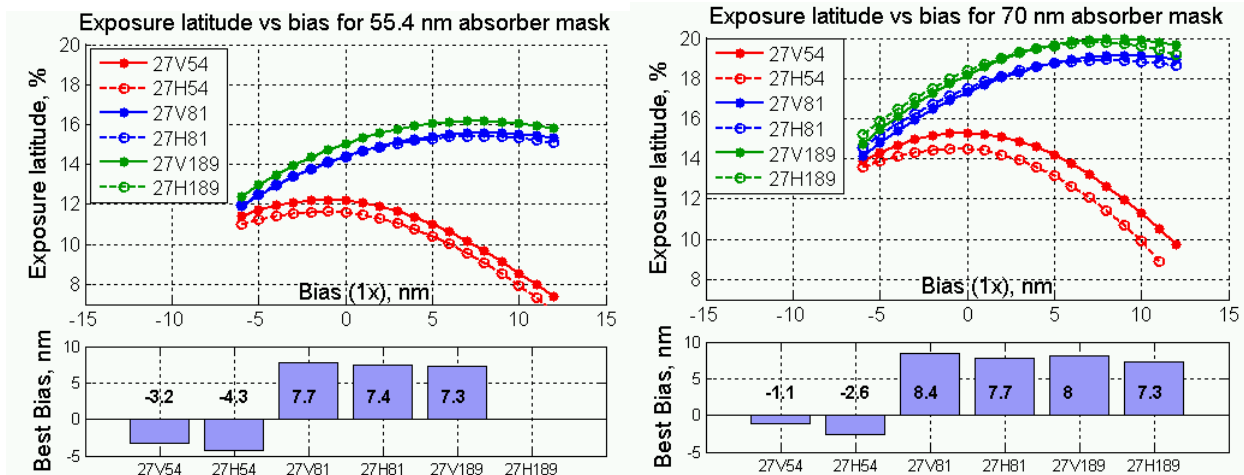


Figure 11 Simulated exposure latitude is shown as a function of mask bias for different LS features for 55.4 nm (left) and 70 nm (right) absorber thickness. $NA=0.25$, $\sigma=0.8$.

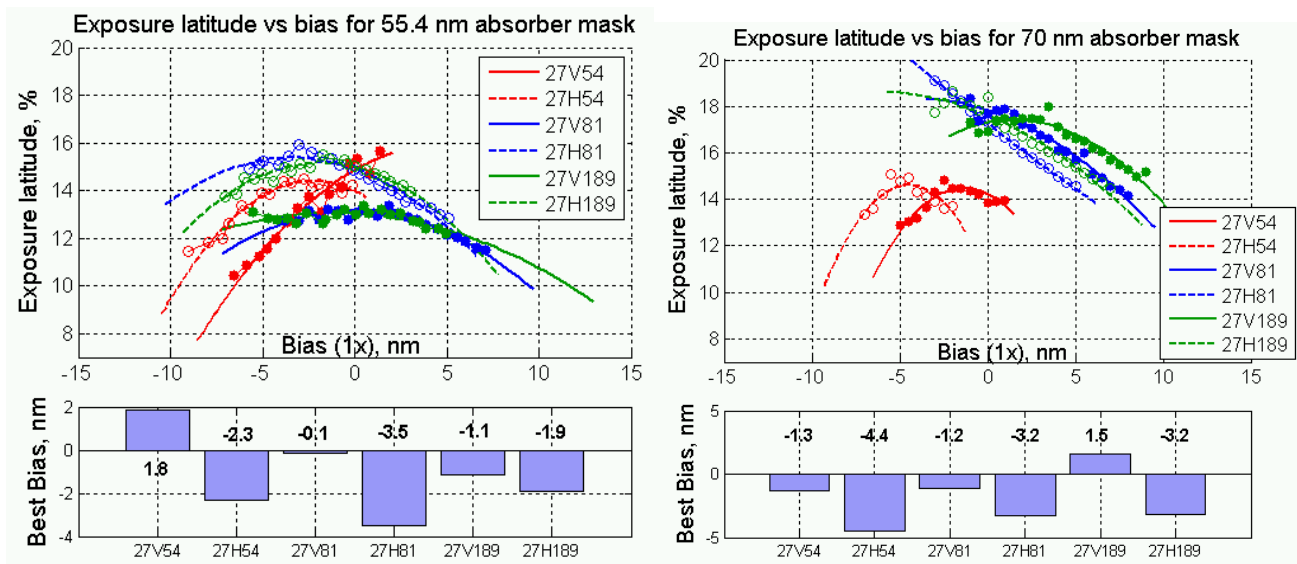


Figure 12 Measured exposure latitude as function of feature bias for 27 nm LS for 55.4 nm (left) and 70 nm (right) absorber heights. Experimental points and quadratic fit are shown. $NA=0.25$, $\sigma=0.8$. Process with the underlayer.

A summary for two masks and two processes is shown in Figure 13. For most of the features and both processes, exposure latitude is higher for 70 nm mask as was expected from simulations. Dose to size is only slightly larger for 70 nm absorber. MEEF is also found to be slightly larger for 70 nm absorber. As expected and shown in multiple publications (see e.g.^[6]), HV bias is larger for 70 nm absorber mask: -2.7 nm compared to -1.7 nm for 55.4 nm mask. Summarizing the results, we can conclude that absorber height preference depends on detailed CDU and contrast budget. For a good quality mask with low mask CDU and with an adequate shadowing correction, thicker absorber performs better. This conclusion is confirmed by other experimental results^{[4],[5]}.

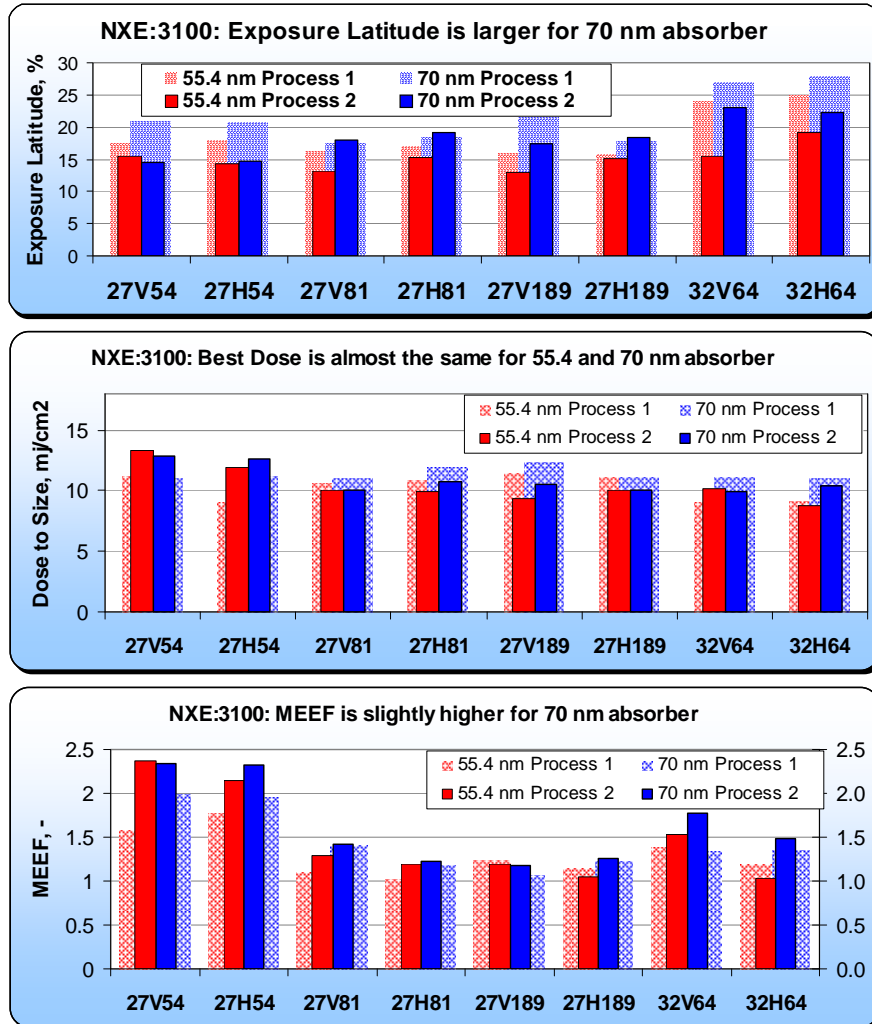


Figure 13 Measured exposure latitude (top), dose to size (middle) and MEEF (bottom) for 55.4 nm and 70 nm absorber mask and two resist processes.

5. IMAGE BORDER FIELD TO FIELD REFLECTIONS

It is known that the reducing of absorber height can essentially reduce shadowing effect^[6]. However, this reduction has a side effect that is an increased reflectivity of absorber, in particular in mask black border areas, that is a 2-3 mm wide absorber area around the image field serving as shield from field-to-field stray light. The increase of the absorber reflectivity results in higher amount of the field-to-field stray light due to parasitic reflections^{[7],[8]}.

This effect has been demonstrated for 44 nm absorber mask exposed on EUV Alpha tool^{[3],[9]}. Here we present a similar experiment performed on NXE:3100 tool and 55.4 nm absorber. A part of the mask was exposed in such a manner that the distance between adjacent fields on the wafer was growing from 0 to 3 mm. Several blocks with the same distances are exposed to be used for averaging (Figure 14).

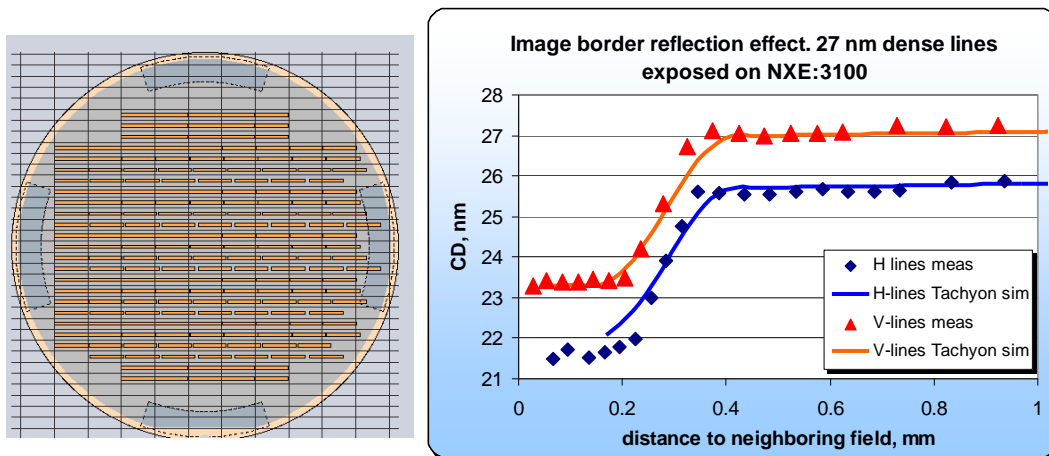


Figure 14 Wafer layout of the die-spacing experiment (left) and the results of the experiment and Tachyon simulation (right). CD drop of about 4 nm is observed for small distances between fields.

Several biases of 27 nm horizontal dense lines were measured. The results of the experiment are shown in Figure 14 (right). CD drop of 3.9 nm was observed for vertical lines and of 4.6 ± 0.4 nm for different horizontal lines biases. Therefore vertical lines are less sensitive to the effect, also horizontal lines with larger negative bias show smaller sensitivity (Figure 15). Notice that nominal design CD is shown, actual mask CD may differ.

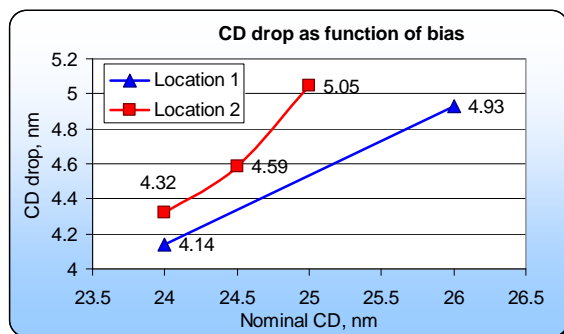


Figure 15 CD drop due to field to field reflections as function of mask bias measured at two different locations in the field. Lines with larger negative bias are less sensitive to the effect.

It follows from the experiment that a safe distance of sensitive structure from the edge of the neighboring field should be about 400 μm . The transition region determined by a half-shadow of Reticle Masking Blades is about 200 μm .

To prevent a CDU impact from field-to-field flare, the mask black border should have very low EUV reflectivity ($< 0.2\%$), which can only be achieved by absorber stack optimization (for example, using a very thick absorber), a special coating, double absorber technique or etching away the entire ML in the black border area^{[10],[11]}. However, the CD impact can also be minimized by means of OPC, using information about exposure tool geometry and layout and also knowledge of absorber stack reflectivity. Such a software solution is implemented in Brion Tachyon OPC.

The image border effect measured on NXE:3100 is simulated by the Tachyon EUV model, as shown in Figure 14 (right). The transition region and the CD drop were reproduced in simulation. This shows potential possibility of mask OPC correction for the image border reflection effect.

The image border effect accumulates in the corners of the image field because reflections from three neighboring fields are summed up there. It was shown in an NXE:3100 experiment that the cumulative CD drop in the corners is larger than 7.5 nm for 70 nm absorber mask and 30 nm dense lines^[12].

6. SUMMARY AND DISCUSSION

Several aspects of mask contribution to imaging were considered. In particular, the impact of mask centroid wavelength on apodization, telecentricity and CD uniformity was shown. The optimal centroid wavelength of ML blank was determined based on detailed scanner spectrum aware simulation simulations with a rigorous 3d mask model calibrated on measured data. This centroid wavelength was found to be 13.52 ± 0.01 nm based on ML reflectivity uniformity metrics and 13.54 ± 0.01 nm based on apodization minimization. This confirms earlier ASML recommendation 13.53 nm for centroid wavelength. Preliminary CD uniformity simulations are performed indicating that CDU impact of ML thickness variation can be essentially reduced if the centroid wavelength is optimized. However pattern placement simulations show that telecentricity might go out of specification for future nodes. More detailed spectral simulations will follow.

We have continued the investigation^[3] of absorber height and bias impact on imaging by means of simulations with the calibrated mask model and by means of NXE:3100 exposures. In particular, the simulations show that larger absorber heights give advantage in exposure latitude for larger angular illumination (higher NA σ) for 27 nm node. In other words, increase in absorber volume provides better optical contrast in case of off axis illumination. This effect was confirmed with NXE:3100 experiment showing higher exposure latitude for 70 nm absorber mask compared to 55.4 nm mask for 27 nm dense, semi-dense and isolated lines. This study shows that there is no immediate need to go to smaller absorber height for future nodes if proper shadowing bias is applied on the mask.

Also the study^{[3],[9]} on image border reflections was continued. It was shown by NXE:3100 experiments that image border reflections can cause CD drop of about 4 nm of 27 nm dense lines at the edge of the field for 55 nm absorber mask with 1.4% reflectance. This effect was reproduced by Brion Tachyon simulations showing a correction potential by means of mask OPC.

7. ACKNOWLEDGEMENTS

The authors would like to thank Johannes Ruoff and Peter Huber from Carl Zeiss Oberkochen for providing optical system data for simulations. We thank Gian Lorusso and Eric Hendrickx from IMEC and Franklin Kalk and Hiroaki Morimoto from Toppan for fruitful cooperation and discussions. We thank Yasuko Saito from Brion for image border effect simulation support. We thank many colleagues at ASML for providing data, wafers, exposure and measurement support and for discussions: Bert Vleeming, Stuart Young, Jo Finders, Friso Wittebrood, Cheuk Wah-man, Marieke van Veen, Vidya Vaenkatesan, Yin Fong Choi, Andre van Dijk.

8. REFERENCES

- [1] Seo, H.S., Park, J., Lee, S.Y., Park, J.O., Kim, H., Kim, S.S. and Cho, H.K., "Properties of EUVL masks as a function of capping layer and absorber stack structures," Proc. of SPIE, Vol. 6517 (2007).
- [2] Ruoff, J., "Impact of mask topography and multilayer stack on high NA imaging of EUV masks," Proc. SPIE, 7823, 78231N (2010).
- [3] Davydova, N.V., van Setten, E., de Kruif, R., Oorschot, D., Dusa, M., Wagner, C., Jiang, J., Liu, W., Kang, H., Liu, H., Spies, P., Wiese, N., Waiblinger, M., "Imaging performance improvements by EUV mask stack optimization," Proc. SPIE, 7985, 79850X (2011).
- [4] McIntyre, G., Zuniga, C., Gallagher, E., Whang, J., Kindt, L., "The trade-offs between thin and thick absorbers for EUV photomasks," Proc. SPIE, 8166-143 (2011).
- [5] Tanabe, H., Murachi, T., Lee, S.H., Chandhok, M., Park, S., Zhang, G., Abe, T., Ogase, T., Hayashi, N., "Phase-shifting effect of thin-absorber EUV masks," Proc. SPIE, 8166-33 (2011).
- [6] van Setten, E., Man, C.W., Murillo Vallejo, R., Lok, S., van Ingen Schenau, K., Feenstra, K., Wagner, C., "Impact of mask absorber on EUV imaging performance," Proc. SPIE, Vol. 7545 (2010).
- [7] Seo, H.S., Lee, D.G., Ahn, B.S., Koh, C.W., Kang, I.Y., Kim, T.G., Kim, H., Kim, D., Kim, S.S. and Cho, H.K., "Absorber stack optimization in EUVL masks: lithographic performances in alpha demo tool and other issues," Proc. SPIE, Vol. 7636 (2010).
- [8] Hyun, Y., Park, J., Koo, S., Kim, Y., Ban, K., Kim, S., Lim, C., Yim, D., Kim, H. and Park, S., "Feasibility of EUVL thin absorber mask for minimization of mask shadowing effect," Proc. of SPIE, Vol. 7636, 763614-1 (2010).
- [9] van Setten, E., Oorschot, D., Man, C.W., Dusa, M., de Kruif, R., Davydova, N.V., Feenstra, K., Wagner, C., Spies, P., Wiese, N., Waiblinger, M., "EUV mask stack optimization for enhanced imaging performance," Proc. SPIE, 7823, 78231O (2010).
- [10] Kamo, T., Aoyama, H., Arisawa, Y., Tawarayama, K., Tanaka, T. and Suga, O., "Thin absorber EUV mask with light-shield border of etched multilayer and its lithographic performance," Proc. SPIE, Vol. 7748, 774805 (2010).

- [11] Kamo, T., Aoyama, H., Tanaka, T., Suga, O., Abe, T., Takikawa, T., Hayashi, N., Shoki, T., Usui, Y. and Hosoya, M., "EUVL practical mask structure with light shield area for 32nm half pitch and beyond," Proc. of SPIE, Vol. 7122, 712227-1 (2008).
- [12] Driessen, F. A. J. M., Davydova, N.V., Jiang, J., Kang, H., Vaenkatesan, V., Oorschot, D., Kim, I.S., Kang, S.N., Lee, Y., Yeo, J., Gronlund, K., Liu, H.Y., van Ingen-Schenau, K., Peeters, R., Wagner, C., Zimmermann, J., Schumann, O., "Holistic lithography for EUV: NXE:3100 characterization of first printed wafers using an advanced scanner model and scatterometry," Proc. SPIE, 8166-23 (2011).